Kinetic modeling of NO_X storage and reduction using spatially resolved MS measurements

Soran Shwan [a], William Partridge [c], Jae-Soon Choi [c], Louise Olsson [a,b,∗]

[a] Competence Centre for Catalysis, Chalmers University of Technology, Gothenburg, Sweden
[b] Chemical Engineering, Chalmers University of Technology, Gothenburg, Sweden
[c] Oak Ridge National Laboratory, Oak Ridge, Tennessee, USA

ABSTRACT

A global kinetic NO_X Storage and Reduction (NSR) Model based on flow reactor experiments was developed to investigate the NO_X storage and reduction mechanisms with a focus on the breakthrough of NH_3 and N_2O during the rich phase. Intra-Catalyst Storage and Reduction Measurements (SpaciMS) were used to further validate the model, particularly with respect to the formation and utilization of ammonia along the catalyst axis. Two different catalysts were used in the model, denoted Cat. 1 and Cat. 2. The first catalyst was used in flow reactor experiments to create a global kinetic model and fitting the parameters using long NSR cycles validated against more realistic short NSR cycles, while the second catalyst was used in the SpaciMS experiments. However, due to some differences in the catalytic material, some parameters had to be re-tuned for the second catalyst. Two NO_X storage sites were used for both catalysts, barium (Ba) and the support sites (S2). Furthermore, the shrinking-core model was used to describe the mass transport of NO_X inside the storage particles, S2. An oxygen storage component was necessarily included and denoted Ce for the first catalyst and representing ceria in the catalyst. The second catalyst did not contain any ceria, which is why the oxygen storage site was called S3 and can be interpreted as oxygen on the noble metal. During the rich period, NO_X was reduced by H_2 and CO, forming nitrogen and NH_3. Produced NH_3 reacted with stored NO_X forming N_2O and resulting in an N_2O peak before NH_3 breakthrough. The model agreed well with reactor experiments and SpaciMS measurements. The SpaciMS results showed that most NO_X was stored in the first half of the catalyst, resulting in high ammonia production in the catalyst front and its subsequent consumption along the catalyst axis to reduce NO_X stored downstream.

© 2013 Elsevier B.V. All rights reserved.

1. Introduction

The products formed during the burning process of internal combustion engines are major contributors to global air pollution, and CO, HC and NO_X are the major components regulated in many countries. The three-way catalyst (TWC) can efficiently convert these compounds to benign species for gasoline stoichiometric engines. However, the emissions from diesel engines and lean burning gasoline engines have a large excess of oxygen. Due to the oxygen competing for a limited amount of reductants, TWCs cannot achieve reasonable NO_X reduction in lean emissions. One solution to this problem is the use of NO_X Storage and Reduction (NSR) catalysts, which was developed by Toyota in the 1990s [1]. In this concept, the catalyst is exposed to mixed lean-rich operation composed of relatively long lean (oxygen excess) pulses, followed

by short rich (oxygen deficient) pulses. NO_X is stored by the catalyst during the lean period and is released and reduced by short rich pulses, thereby regenerating the storage component. During the rich period, NO_X is reduced with hydrocarbons (HC), H_2 and CO, to produce CO_2, H_2O and N_2. Furthermore, due to H_2 and HC in the rich period [2–4], NH_3 and N_2O may also be produced. Ammonia slip from NSR catalysts has been observed [5–12] during operation, and is a major problem for urban air quality [13]. NH_3 forms secondary aerosols which are important contributors to urban fine particulate (PM2.5) pollution [14]. Although as yet an unregulated emission, N_2O has 300-times greater greenhouse potential than CO_2 on an equivalent-mass basis, and 5% of all U.S. greenhouse gas emissions from human activities [15]. Due to NH_3 and N_2O slip, strategies to minimize nitrogen-containing emissions other than N_2 are desirable.

The NSR catalyst usually consists of a high surface area support, a storage component and a precious metal. The Pt/Ba/Al catalyst has been a well-studied system. Szailer et al. [16] showed that during the rich period, the main role of H_2 is to keep the precious metal

∗ Corresponding author.
   E-mail address: louise.olsson@chalmers.se (L. Olsson).

Nomenclature list

A_i	pre-exponential factor for reaction i. Depends on the rate expression
C_k	mole fraction at the reaction layer of species k (−)
C_k^B	mole fraction in the bulk gas of species k (−)
d_{hyd}	hydraulic diameter of the channel (m)
$D_{k,g}$	diffusion coefficient of species k in the gas mixture
$E_{a,i}$	activation energy for reaction i (J/mol)
ΔG	Gibbs free energy (kJ/mol)
GSA	geometric surface area per reactor volume (m^{-1})
ΔH	enthalpy change (kJ/mol)
$k_{k,m}$	mass transfer coefficient of species k (mol/m^2 s)
K	equilibrium constant (−)
k_i	rate constant for reaction i. Depends on the rate expression
l	thickness of the nitrate or nitrite layer
$MG_{k,g}$	molar mass of gas phase species k (kg/kmol)
r	radius of particle
r_1	radius of the particle reaction front
r_{tot}	total radius of particle
r_i	reaction rate for reaction i (kmol/s m$^3_{washcoat}$)
R	gas constant (J/mol K)
R_{diff}	rate of diffusion (mol/s m^2)
S	sensitivity (%)
ΔS	entropy change (J/mol K)
Sh	Sherwood number (−)
T_s	temperature at catalyst surface (K)
t	time (s)
$\upsilon_{k,i}$	stoichiometric coefficient of species k in reaction i
υ_g	gas velocity
$w_{k,g}$	mass fraction of species k in gas phase (−)
z	spatial coordinate in axial direction (m)

Greek letters

γ	conversion factor (m^{-1})
ε_g	volume fraction of gas phase in entire system (−)
θ_k	coverage of specie k (−)
ρ_g	density of the gas phase (kmol/m^3)
Θ_j	surface site density of storage site j (mol/m^2)

clean for dissociation of NO$_X$ by reacting with adsorbed oxygen to form H$_2$O. Furthermore, it was suggested that the formation of NH$_3$ occurs due to adsorbed nitrogen atoms reacting with H$_2$. The selectivity of the formed NSR products was studied by Pihl et al. [17], who found that the formation of NH$_3$ was favored when the ratio of reductant to NO$_X$ was high and the temperature low. Furthermore, knowing that NH$_3$ is an effective reductant for both NO and NO$_2$ [7], Pihl et al. observed that NH$_3$ formed in the front parts of the catalyst at low temperatures was partially consumed further into the catalyst via regeneration reactions or the reduction of stored oxygen [17].

Studies to better understand ammonia formation from NSR catalysts have been driven by the need to avoid NH$_3$ slip. Clayton et al. [12] showed that by progressively shortening the catalyst sample, H$_2$ was reacting with stored NO$_X$ to form NH$_3$ and then reduced downstream of the catalyst with stored NO$_X$. Partridge et al. [18] further studied the intra-ammonia formation using Spatially Resolved Capillary Inlet Mass Spectrometry (SpaciMS). Transient NH$_3$, NO$_X$, N$_2$ and H$_2$ distributions within an operating NSR catalyst at different operating temperatures were studied. The results showed three distinct NH$_3$ zones, a build-up zone in the front section of the catalyst, a balance zone, in addition to a zone at the back-end of the catalyst. More ammonia was generated

than consumed in the front zone of the catalyst where most of the NO$_X$ was stored. However, downstream of the build-up zone, where remaining NO$_X$ was stored, there was a balance between NH$_3$ production and reduction. Furthermore, the data showed that at the back-end of the catalyst, which did not show any significant NO$_X$ storage, a depletion zone existed where ammonia was consumed by surface oxygen. According to Partridge et al. [18], the SpaciMS results showed that there is a complex reaction network in the catalyst, mainly in the front, including NH$_3$ generation, H$_2$ and NH$_3$ reduction, as well as parallel direct-H$_2$ and intermediate-NH$_3$ regeneration pathways.

There are multiple kinetic models describing the NSR process in the literature [12,19–29]. Olsson et al. [19,20], Tuttlies et al. [22] and Hepburn et al. [29] used global kinetic models to describe the NO$_X$ storage and reduction, where a shrinking-core model was used to describe the mass transport. Lindholm et al. [21] developed a detailed NSR kinetic model to describe the storage and regeneration using hydrogen, which also included ammonia formation over a Pt/Ba/Al catalyst. In this study, the reaction between stored NO$_X$ and NH$_3$, according to SCR chemistry, was added.

However, to our knowledge, there are no kinetic models for NO$_X$ storage that have presented intra-catalyst concentrations and been verified by experiments using intra-catalyst measurements in the open literature. The objective of this study was to use both flow reactor experiments and SpaciMS to further investigate the mechanism of NO$_x$ storage and reduction over barium containing NSR catalysts using a global kinetic model focusing on NH$_3$ and N$_2$O breakthroughs. A Global Kinetic NSR Model was developed based on long experimental NSR cycles and validated against short experimental NSR conducted by Pihl et al. [17]. The simulated intra-catalyst concentration was thereafter verified with the help of SpaciMS measurements by Partridge et al. [18] to investigate the intra-catalyst concentrations during storage and reduction of NO$_X$, as well the formation and reduction of ammonia.

2. Experimental

Two different catalysts were used in the present study. Catalyst 1 is a Commercial Gasoline Direct Injection (GDI) LNT Catalyst manufactured by Umicore (Auburn Hills, MI). The major washcoat components include alumina, ceria, zirconia, and barium. The washcoat also contains platinum, palladium, and rhodium at a ratio of 82:26:6 and a total loading of 3990 g/m^3. The surface area of the material (including substrate) was determined by N$_2$ adsorption resulting in 27.1 m^2/g. More details about the catalyst can be found in Ref. [17]. A second catalyst, Catalyst 2, provided by EmeraChem (Knoxville, TN), was also used in this study to validate the model against spatially resolved measurements, SpaciMS. The material was a Pt/Ba/Al$_2$O$_3$ model LNT catalyst washcoated on a honeycomb cordierite monolith (46.5 cells per cm^2). The Pt and BaO loadings were 6.2 and 15 g/L. The surface area of the catalyst was determined to be 14 m^2/g from Ar adsorption at 77 K. Further details on the catalyst can be found in Ref. [18].

Catalyst 1 was used in bench-scale flow reactor experiments, where long and short NSR experiments were performed. The long cycles consisted of 900 s lean periods and 600 s rich periods conducted over the 200–500 °C temperature interval. During the lean period, the sample was exposed to 300 ppm of NO, 10% O$_2$, 5% H$_2$O and 5% CO$_2$ with nitrogen as balance. During the rich period, the sample was exposed to 375 ppm H$_2$, 625 ppm CO, 5% H$_2$O and 5% CO$_2$ with nitrogen as balance. Short cycles were conducted with 60 s lean periods and 5 s rich periods in the 200–500 °C temperature interval. During the lean period, the sample was exposed to 300 ppm of NO, 10% O$_2$, 5% H$_2$O and 5% CO$_2$, with nitrogen as balance. During the rich period, the sample was exposed to 2700 ppm

H_2, 4500 ppm CO, 5% H_2O and 5% CO_2 with nitrogen as balance. More details about the flow reactor experiments can be found in Ref. [17].

Intra-catalyst gas phase speciation was performed using SpaciMS measurements. The Catalyst 2 described earlier was used in these experiments. The intra-catalyst capillary and thermocouple were positioned in adjacent catalyst channels. In addition to the catalyst inlet (at 0.0 mm) and outlet measurements (76.2 mm), intra-catalyst channel measurements were made at 11 locations; these measurements were from the inlet face at 3.2, 6.4, 9.5, 12.7, 15.9, 19.0, 28,6, 38.1, 47.6, 57.2 and 66.7 mm. Measurements were made at m/z 2 (H_2), m/z 14 (N_2, NH_3, NO_X = NO + NO_2), m/z 15 (NH_3, NO_X), m/z 30 (NO_X) and m/z 84 (Kr). Short cycles were performed during the SpaciMS measurements, with 60 s lean periods and 5 s rich periods conducted at 325 °C. During the lean period, the sample was exposed to 300 ppm of NO, 10% O_2, 5% H_2O and 5% CO_2 with Ar as balance and Kr as an internal standard. During the rich period, the sample was exposed to 2% H_2, 5% H_2O and 5% CO_2 with Ar as balance and Kr as an internal standard. More details on the SpaciMS measurements are found in Ref. [18].

3. Model

3.1. Reactor model

A commercial program, AVL BOOST [30], was used in combination with user defined files in FORTRAN to conduct kinetic modeling, as used previously in our group [31,32]. The ideal gas law was applied and all gas properties were evaluated depending on the temperature, pressure and gas composition. The channel was discretized longitudinally into 15 grid-points, where all the equations including reactions were solved.

The assumptions made for the reactor model were:

i. Uniform radial flow distribution across the monolith.
ii. No diffusion resistance in the washcoat.
iii. The average coverage of the surface was used to model surface adsorption at each grid-point.
iv. No heat balances were solved. The temperature gradients during long NSR cycles were only about 5–12 °C during the rich period, and only small effects of the exotherms are expected in the simulations. However, note that the temperature gradients for the short NSR cycles, used for validation, were about 10–25 °C, which may affect the results slightly. This is further discussed in the results section.

The main governing equation for the gas phase species in a single channel model is [30]:

$$\varepsilon_g \frac{\partial \rho_g \cdot w_{k,g}}{\partial t} = \varepsilon_g \frac{\partial \rho_g \cdot w_{k,g} \cdot \upsilon_g}{\partial z} + MG_{k,g} \sum_i^{nr} \upsilon_{i,k} \cdot r_i \left(C_k, T_s, \theta_k \right) \tag{1}$$

The coverage of component k on the surface is solved by [30]:

$$\frac{\partial \theta_k}{\partial t} \left(\Theta \cdot GSA \right) = \sum_i^{nr} \upsilon_{i,k} \cdot r_i(C_k, T_s, \theta_k) \tag{2}$$

The geometric surface area per unit reactor volume, GSA, in Eq. (2) is given by [30]:

$$\frac{GSA}{d_{hyd}} = 4 \times (cell\ density) \tag{3}$$

Furthermore, mass transport from gas bulk to the catalytic surface and vice-versa was included. Under quasi steady-state conditions, the rates of the surface reactions balanced the diffusive

transport from the gas bulk to the surface. The molar surface concentration (C_k) of component k was evaluated using [30]:

$$GSA \cdot k_{k,m} \cdot \left(C_k - C_k^B \right) = \sum_i^{nr} \upsilon_{i,k} \cdot r_i \left(C_k, T_s, \theta_k \right) \tag{4}$$

where C_k^B was the concentration of species k in the gas bulk and $k_{k,m}$ was the mass transfer coefficient of the individual species calculated according to [30]:

$$k_{k,m} = \frac{Sh \cdot D_{k,g}}{d_{hyd}} \tag{5}$$

where $D_{k,g}$ was the diffusion coefficient of species k in the gas mixture and the Sherwood number was calculated according to the Sieder/Tate relationship [33].

3.2. Kinetic model

To simulate and capture the temperature dependence in the kinetic model, the Arrhenius equation was used for rate constants k,

$$k_i = A_i e^{-E_{A_i}/RT_s}. \tag{4}$$

The model used in this study was divided into three sub-models: (i) NO oxidation and water–gas shift reaction, (ii) storage of different gas species during the lean period, and (iii) catalyst regeneration during the rich period. These sub-models describe the steps occurring over the LNT catalyst during NO_X storage and reduction with hydrogen and carbon monoxide as reducing agents. The sub-models were developed stepwise and described below. All mechanisms for the sub-models are listed in Tables 1–3.

A sensitivity analysis of the kinetic parameters fitted for long NSR cycles at 300 °C and 500 °C was performed to study the relative sensitivity of each parameter on the simulation. All the parameters are increased and decreased by 1% where the residual between the measured and simulated values of NO_X, N_2O, NH_3 and CO are calculated summarized. The sensitivity for each parameter is calculated according to,

$$S^2 = \sum \left[\left(NO_X^{measured} (ppm) - NO_X^{simulated} (ppm) \right)^2 \right.$$
$$\left. + \cdots + \left(CO^{measured} (ppm) - CO^{simulated} (ppm) \right)^2 \right]$$

where the upper och lower limits are presented in Tables 5–7 according to,

$$S = \left| \frac{S_{original} - S_{changed}}{S_{original}} \right| \times 100. $$

3.3. NO oxidation and water–gas shift reaction

Previous studies [23] have shown that NO oxidation to NO_2 on noble metal sites is an important reaction step in NSR catalysts. It was likewise suggested that NO oxidation is the rate-determining step for NO_X storage at lower temperatures [34]. According to Olsson et al. [20], a reversible global NO oxidation step was used where the equilibrium constant was calculated based on the change in Gibbs free energy,

$$K_{eq} = e^{-\Delta G/RT} \tag{5}$$

where

$$\Delta G = \Delta H - T\Delta S \tag{6}$$

The values for the enthalpy and entropy changes were set according to Olsson et al. [20], to $\Delta H = -58$ kJ/mol and

Table 1
Reactions and rate expressions for; NO oxidation and water gas shift reaction and; NO_X adsorption and desorption over barium and S2, and oxygen storage over ceria and S3.

Nr	Reaction	Reaction rate
1	$NO + \frac{1}{2}O_2 \Leftrightarrow NO_2$	$r_1 = k_1 C_{O_2}^{0.5} C_{NO} - \frac{k_1}{K_{eq,1}} C_{NO_2}$
2	$H_2O + CO \Leftrightarrow CO_2 + H_2$	$r_2 = k_3 C_{H_2O} C_{CO} - \frac{k_3}{K_{eq,1}} C_{CO_2} C_{H_2}$
3	$\frac{1}{2}BaCO_3 + NO_2 + \frac{1}{4}O_2 \Leftrightarrow \frac{1}{2}Ba(NO_3)_2 + \frac{1}{2}CO_2$	$r_3 = k_5 C_{NO_2} C_{O_2}^{1/4} \theta_{BaCO_3} - \frac{k_5}{K_{eq,3}} C_{CO_2}^{1/2} \theta_{Ba(NO_3)_2}$
4	$\frac{1}{2}BaCO_3 + NO + \frac{1}{4}O_2 \Leftrightarrow \frac{1}{2}Ba(NO_2)_2 + \frac{1}{2}CO_2$	$r_4 = k_7 C_{NO} C_{O_2}^{1/4} \theta_{BaCO_3} - \frac{k_7}{K_{eq,4}} C_{CO_2}^{1/2} \theta_{Ba(NO_2)_2}$
5	$S2 + NO_2 \Leftrightarrow S2 - NO_2$	$r_5 = k_9 C_{NO_2} \theta_{S2} - \frac{k_9}{K_{eq,5}} \theta_{S2-NO_2}$
6	$S2 + NO \Leftrightarrow S2 - NO$	$r_6 = k_{11} C_{NO} \theta_{S2} - \frac{k_{11}}{K_{eq,6}} \theta_{S2-NO}$
7[a]	$CeO_{1.5} + \frac{1}{4}O_2 \rightarrow CeO_2$	$r_7 = k_7 C_{O_2}^{1/4} \theta_{CeO_{1.5}}$
8[b]	$S3 + \frac{1}{2}O_2 \rightarrow S3 - O$	$r_8 = k_8 C_{O_2}^{1/2} \theta_{S3}$

[a] – active only for Cat.1.
[b] – active only for Cat.2.

$\Delta S = -76.1$ J/(mol K). The reaction and corresponding rate are shown in Table 1.

Hydrogen was present in the exhaust gas during the rich operation and could also be catalytically produced by the water–gas shift reaction [35] of CO and H_2O. Similar to NO oxidation and according to Koci et al. [36], a reversible global reaction step was used where the values for the enthalpy change and entropy change were set at $\Delta H = 38.862$ kJ/mol and $\Delta S = -37.1633$ J/mol K [37]. The reaction step for the water–gas shift reaction is summarized in Table 1.

3.4. NO_X storage

The NO_X storage sub-model is based on the shrinking-core model developed by Olsson et al. [20,25]. The mechanism contains four reversible reaction steps, where NO_X was stored over two types of storage sites, $BaCO_3$ and S2. Several studies suggest different types of storage sites in NO_X storage catalysts [38–42]. Temperature programmed desorption experiments of NO_X over Pt/Ba/Al showed several desorption peaks [43]. This was explained by different NO_X species of varying storage strength on the surface or different types of storage sites. Westerberg and Fridell [44] assigned the peaks to different nitrites and nitrates on barium. Furthermore, ceria/zirconia/alumina, which often act as support for the storage material, can also adsorb NO_X and thereby increase the NO_X storage capacity [44,45]. In the present model, NO_X storage is described by reversible adsorption of nitrates and nitrites over Ba and a second site, S2. Several oxidizing steps of nitrites to nitrates have been proposed [21]. To simplify the model, these steps have been omitted in the simulation. However, we would like to emphasize that this does not mean that oxidation reactions do not occur, but are only a simplification of the global model. In earlier kinetic models [21,25], it was discovered that it is crucial to have two sites for NO_X storage; one site at low temperature and another site at higher temperature. In the present model, although S2 also stores at 400 °C, S2 has the primary storage at lower temperature. The physical interpretation of S2 might be alumina and ceria. In addition, it has been suggested that NO_X stores on barium, forming different species with different binding strength. Therefore, some

Table 2
Reactions and rate expressions for NH_3 production and reduction and N_2O production.

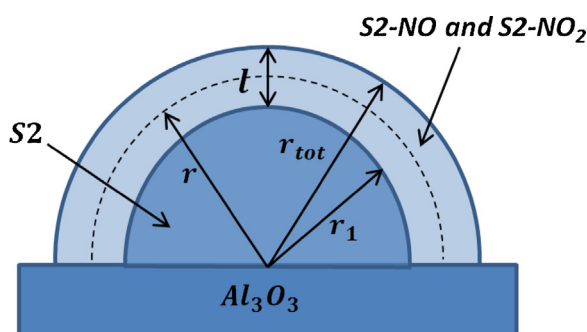|		
9	$Ba(NO_3)_2 + 8H_2 + CO_2 \rightarrow BaCO_3 + 2NH_3 + 5H_2O$	$r_9 = k_9 C_{CO_2} C_{H_2} \theta_{Ba(NO_3)_2}$
10	$Ba(NO_2)_2 + 6H_2 + CO_2 \rightarrow BaCO_3 + 2NH_3 + 3H_2O$	$r_{10} = k_{10} C_{CO_2} C_{H_2} \theta_{Ba(NO_2)_2}$
11	$2S2-NO_2 + 7H_2 \rightarrow 2S2 + 2NH_3 + 4H_2O$	$r_{11} = k_{11} C_{H_2} \theta_{S2-NO_2}$
12	$2S2 - NO + 5H_2 \rightarrow 2S2 + 2NH_3 + 2H_2O$	$r_{12} = k_{12} C_{H_2} \theta_{S2-NO}$
13	$\frac{3}{2}Ba(NO_3)_2 + 5NH_3 + \frac{3}{2}CO_2 \rightarrow \frac{3}{2}BaCO_3 + 4N_2 + 7.5H_2O$	$r_{13} = k_{13} C_{NH_3} C_{CO_2} \theta_{Ba(NO_3)_2}$
14	$Ba(NO_2)_2 + 2NH_3 + CO_2 \rightarrow BaCO_3 + 2N_2 + 3H_2O$	$r_{14} = k_{14} C_{NH_3} C_{CO_2} \theta_{Ba(NO_2)_2}$
15	$2S2 - NO_2 + 2NH_3 + H_2 \rightarrow 2N_2 + 2S2 + 4H_2O$	$r_{15} = k_{15} C_{NH_3} C_{H_2} \theta_{S2-NO_2}$
16	$6S2 - NO + 4NH_3 \rightarrow 5N_2 + 6S2 + 6H_2O$	$r_{16} = k_{16} C_{NH_3} \theta_{S2-NO}$
17	$Ba(NO_3)_2 + 2NH_3 + CO_2 \rightarrow BaCO_3 + 2N_2O + 3H_2O$	$r_{17} = k_{17} C_{CO_2} C_{NH_3} \theta_{Ba(NO_3)_2}$
18	$2Ba(NO_2)_2 + 2NH_3 + 2CO_2 \rightarrow 2BaCO_3 + 3N_2O + 3H_2O$	$r_{18} = k_{18} C_{CO_2} C_{NH_3} \theta_{Ba(NO_2)_2}$
19	$8S2-NO_2 + 6NH_3 \rightarrow 8S2 + 7N_2O + 9H_2O$	$r_{19} = k_{19} C_{NH_3} \theta_{S2-NO_2}$
20	$8S2 - NO + 2NH_3 \rightarrow 8S2 + 5N_2O + 3H_2O$	$r_{20} = k_{20} C_{NH_3} \theta_{S2-NO}$

Table 3
Reactions and rate expressions for regeneration of barium, S2, ceria and S3 and reduction of NO.

21	$Ba(NO_3)_2 + 3H_2 + CO_2 \rightarrow 2NO + BaCO_3 + 3H_2O$	$r_{21} = k_{21}C_{CO_2}C_{H_2}\theta_{Ba(NO_3)_2}$
22	$Ba(NO_3)_2 + 3CO \rightarrow 2NO + BaCO_3 + 2CO_2$	$r_{22} = k_{22}C_{CO}\ \theta_{Ba(NO_3)_2}$
23	$Ba(NO_2)_2 + H_2 + CO_2 \rightarrow 2NO + BaCO_3 + H_2O$	$r_{23} = k_{23}C_{CO_2}C_{H_2}\theta_{Ba(NO_2)_2}$
24	$Ba(NO_2)_2 + CO \rightarrow 2NO + BaCO_3$	$r_{24} = k_{24}C_{CO}\ \theta_{Ba(NO_2)_2}$
25	$S2 - NO_2 + H_2 \rightarrow NO\ + S2 + H_2O$	$r_{25} = k_{25}C_{H_2}\theta_{S2-NO_2}$
26	$S2 - NO_2 + CO\ \rightarrow NO\ + S2 + CO_2$	$r_{26} = k_{26}C_{CO}\theta_{S2-NO_2}$
27	$S2NO\ \ + H_2 \rightarrow \frac{1}{2}N_2 + S2 + H_2O$	$r_{27} = k_{27}C_{H_2}\theta_{S2-NO}$
28	$S2NO\ \ + CO\ \rightarrow \frac{1}{2}N_2 + S2 + CO_2$	$r_{28} = k_{28}C_{CO}\theta_{S2-NO}$
29[a]	$2CeO_2 + CO \rightarrow CO_2 + 2CeO_{1.5}$	$r_{29} = k_{29}C_{CO}\theta_{CeO_2}$
30[a]	$2CeO_2 + H_2 \rightarrow H_2O + 2CeO_{1.5}$	$r_{30} = k_{30}C_{H_2}\theta_{CeO_2}$
31[b]	$S3 - O + H_2 = H_2O + S3$	$r_{31} = k_{31}C_{H_2}\theta_{S3-O}$
32[b]	$S3 - O + CO = CO_2 + S3$	$r_{32} = k_{32}C_{CO}\theta_{S3-O}$
33	$NO + H_2 \rightarrow H_2O + \frac{1}{2}N_2$	$r_{33} = k_{33}C_{NO}C_{H_2}$
34	$NO + CO \rightarrow CO_2 + \frac{1}{2}N_2$	$r_{34} = k_{34}C_{NO}C_{CO}$

[a] – active only for Cat.1.
[b] – active only for Cat.2.

NO_x storage on S2 could also be related to barium, which explains why some storage also occurs on S2 at 400 °C, where NO_X storage on alumina is limited. For Ba, the enthalpy change for the equilibrium constant was taken from thermodynamic tables and was not fitted to the experiments [20], while the entropy change was fitted to the experiments. The reason for tuning ΔS is that data in thermodynamic tables are for bulk materials but in our case, we also have surface species. For the second storage site, S2, all parameters were fitted. The reaction steps for NO_X storage are summarized in Table 1.

Internal mass transport within the particles of the NO_X storage material has been included in some NO_X storage simulations [20,25]. There have been mechanisms proposed for which there was mass transport in the washcoat [46] and others where there was mass transport limitation in the particles [29,47]. It is difficult to determine whether there are mass transport limitations in the washcoat or in the storage particles or a combination of the two. Olsson et al. [20] derived a shrinking-core model, similar to the model previously derived by Hepburn et al. [29], which was used in this study to describe mass transport in the storage particle. The nitrates (and nitrites) started to form on the external surface and penetrated into the particle, as shown in Fig. 1, where r_{tot} was the radius of the particle and l the thickness of the nitrate (or nitrite)

layer. The reaction rates are only dependent on the gas-phase concentrations and the coverage of free storage sites at the reaction front at radius r_1. All sites at a radius larger than r_1 were occupied before adsorption could occur deeper into the particle. The following shrinking-core rate expression for formation of nitrites and nitrates on S2 was derived and is shown below. In this study, the shrinking-core rate expression was not used for barium particles because the site density of barium was low compared to the site density of S2. In addition, the storage on barium occurred at higher temperatures, where the storage was dominated by the total uptake and not limited by mass transport in the particles. At low temperatures, the storage was dominated by the S2 site where it was not possible to differentiate the mass transport limitations for barium from those of S2, hence the shrinking-core rate expression was not used for barium in this study. However, it was critical for the storage on S2.

The reaction rate associated with reaction (5) (r_5) in Table 1 can be written as

$$r = r_f + r_b \tag{7}$$

$$r_f = k_f C_{NO_2}^{r=r_1}\theta_{S2} \tag{8}$$

$$r_b = k_b\theta_{S2-NO_2} \tag{9}$$

where $C_{NO_2}^{r=r_1}$ was the concentration of NO_2 at the reaction front $(r = r_1)$ and θ_{S2-No_2} and θ_{S2} were the mean coverage of adsorbed NO_2 over S2 and "free" S2, respectively. The rate of diffusion, R_{diff}, at any radial position r was constant and could be expressed as [20]:

$$R_{diff} = D(4\pi r^2)\frac{dC}{dr} \tag{10}$$

where D was the diffusivity. After integrating between r_1 and r_{tot}, Eq. (10) can be written as

$$R_{diff} = \frac{4\pi D}{l}\left(C_{NO_2}^{r=r_{tot}} - C_{NO_2}^{r=r_1}\right)r_1 r_{tot} \tag{11}$$

Fig. 1. Schematic picture of shrinking-core model. S2-NO and S2-NO₂ formation in S2 particle.

At the interface ($r = r_1$), the rate of diffusion was equal to the rate of reaction, which resulted in:

$$\frac{4\pi D}{l}\left(C_{NO_2}^{r=r_{tot}} - C_{NO_2}^{r=r_1}\right)r_1 r_{tot} = 4\pi r_{tot}^2\left(\frac{k_f}{\gamma}C_{NO_2}^{r=r_1}\theta_{S2} - \frac{k_b}{\gamma}\theta_{S2-NO_2}\right) \tag{12}$$

By rearrangement, the formula provided the following expression of NO_2 at the reaction front:

$$C_{NO_2}^{r=r_1} = \frac{C_{NO_2}^{r=r_{tot}} + k_b\frac{lr_1}{\alpha r_{tot}}\left(\theta_{S2-NO_2}\right)}{1 + k_f\frac{lr_1}{\alpha r_{tot}}C_{NO_2}^{r=r_1}\theta_{S2}} \tag{13}$$

where α was $D \cdot \gamma$, D was the diffusivity, γ a conversion factor and α was tuned in the model.

θ_{S2} is exchanged to $\left(1 - \left(\theta_{S2-NO_2} + \theta_{S2-NO}\right)\right)$ because S2 particles were not only occupied by NO_2 but also by NO. Inserting Eq. (8), (9) and (13) into Eq. (7) resulted in:

$$r = \frac{k_f}{1 + k_f\frac{lr_1}{\alpha r_{tot}}\left(1 - \left(\theta_{S2-NO_2} + \theta_{S2-NO}\right)\right)}C_{NO_2}^{r=tot}C_{O_2}^{\frac{1}{2}}$$

$$- \frac{k_{fb}}{1 + k_f\frac{lr_1}{\alpha r_{tot}}\left(1 - \left(\theta_{S2-NO_2} + \theta_{S2-NO}\right)\right)}\theta_{s2-NO_2} \tag{14}$$

Eq. (14) is the rate expression for NO_2 storage on S2 particles. The thickness of the layer l and the ratio $\frac{r_1}{r_{tot}}$ can be replaced by the following:

$$l = \left[r_{tot}^3 - \left(\theta_{S2-NO_2} + \theta_{S2-NO}\right)r_{tot}^3\right]^{1/3} \tag{15}$$

$$\frac{r_1}{r_{tot}} = \left[1 - \left(\theta_{S2-NO_2} + \theta_{S2-NO}\right)\right]^{1/3} \tag{16}$$

Eqs. (15) and (16) have been derived by rearranging:

$$\theta_{S2-NO_2} + \theta_{S2-NO} = \frac{r_{tot}^3 - r_1^3}{r_{tot}^3} \tag{17}$$

As mentioned above, this derivation will be used to describe the NO_X adsorption and desorption on the different NO_X storage sites for Cat. 1 and Cat. 2. All NO_X storage rates are summarized in Table 1.

3.5. Oxygen storage over ceria and S3

Ceria has shown a high oxygen storage capacity and is a widely used material in exhaust gas catalysis. Ceria has been studied previously as a support material in NSR systems and it was shown that ceria was capable of storing NO_X as well [48–50]. However, it was observed that ceria-supported NSR catalysts have lower NO_X reduction capability than alumina-supported catalysts [48]. Due to the fact that Catalyst 1 contains ceria, an oxygen storage step on ceria was included in our kinetic mechanism. The second catalyst used in this study did not contain any ceria. However, it was crucial to keep the oxygen storage capability in the model for Cat. 2, as well to explain the experimental observations (i.e., some level of oxygen storage/reduction occurring on Cat. 2). Hence an oxygen storage step was included over a third site, S3, for such use instead of ceria. Indeed, Partridge et al. [18] suggested that due to stored oxygen over the Pt sites, there is a high oxygen surface coverage and, therefore, most likely that the S3 represents the Pt sites. The oxygen storage steps are summarized in Table 1.

3.6. Catalyst regeneration and NO_X reduction

3.6.1. NH_3 production/reduction and N_2O formation

During catalyst regeneration, previous experiments have shown that NH_3 and N_2O are common byproducts when reducing NO_X with hydrogen [2,3,7,17]. Pihl et al. [17] performed multiple experiments where NH_3 and N_2O were produced showing that both byproducts were formed from stored NO_X during the regeneration process. The experimental data for Cat. 1 show ammonia and nitrous oxide formation during the rich period for both long and short experiments. Different mechanisms for NH_3 formation during the rich period have been previously proposed, where Koci et al. [24] developed a global NSR model with H_2 and CO as reducing agents, including NH_3 production and reduction during the rich period. Furthermore, Olsson et al. [25] also developed a global model that describes the ammonia production. In the experiments by Pihl et al. [17] and Lindholm et al. [21], the ammonia breakthrough was always delayed but started when the NO_X signal became close to zero. Lindholm et al. [21] proposed that ammonia is produced and reduced with stored NO_X according to the SCR-like chemistry (but in the absence of gas-phase O_2), which causes a delay in the ammonia breakthrough, as observed in the experiments. Furthermore, nitrous oxide was observed before the ammonia peak at the catalyst outlet during the experiments by Pihl et al. [17], showing the need for understanding the pathways for N_2O formation. It was suggested that both NH_3 and N_2O are products derived from stored NO_X. The experiments indicated that N_2O is a byproduct of NH_3 reacting with NO_X. However, Koci et al. [4] recently proposed a mechanism for N_2O formation from produced NH_3 and stored NO_X using selectivity functions in the reaction kinetic to predict N_2O during the rich phase. An NH_3–NO_X reaction was therefore included in the model, where NH_3 reacts with stored NO_X to produce nitrogen and nitrous oxide as byproducts, an outcome in line with the detailed model by Lindholm et al. [21]. In order to accurately predict the N_2O production before the ammonia breakthrough it was crucial in the model to add a reaction step where N_2O was produced directly from stored NO_X and NH_3. Other mechanisms were also examined, but they were not successful. Furthermore, ammonia reduction through oxidation by stored oxygen upstream in the catalyst is also likely to occur [21,51]. However, to keep the model simple, these steps were neither included nor were necessary to describe the simulated evolution of NH_3 compared to the experimental measurements. However, we would like to reemphasize that this does not mean that the reaction does not exist but is only a simplification of the global model. All reaction steps for NH_3 production/reduction and N_2O formation are summarized in Table 2. Note that NO_X reduction by feed reductants such as H_2 and CO could also lead to N_2O as recently proposed [4,51], however it was not included in this model, in order to keep the model as simple as possible.

3.6.2. Regeneration of the storage sites with H_2 and CO

NO_X reduction has been previously shown to occur over the noble metal sites [21]. Lindholm et al. [21] developed a detailed NSR model, where stored NO_X reacts with H_2 to produce both N_2 and NO. The released NO further reacts over the noble metal to produce nitrogen. However, the present global model does not include any NO adsorption over the precious metals, the same approach as previously used in the global models for LNT [24,25]. The present global model includes the regeneration of NO_X storage sites and direct reduction of NO in the gas phase with H_2 and CO as reducing agents similar to the approach by Koci et al. [24]. However, we would like to highlight that this does not mean that a reaction occurs in the gas phase but is only a simplification of a global kinetic step.

Furthermore, regenerating the oxygen storage sites was needed [24,25]. Koci et al. [24] found that regenerating the oxygen sites was crucial for predicting the CO breakthrough outlet concentration. In the present study, regeneration of the oxygen storage sites, ceria and S3, according to Koci et al. [24] were thus included with H_2 and
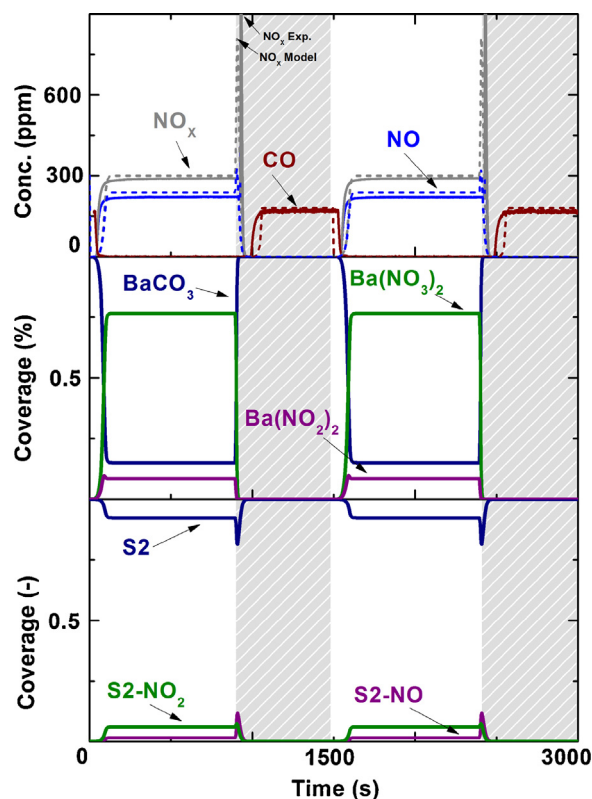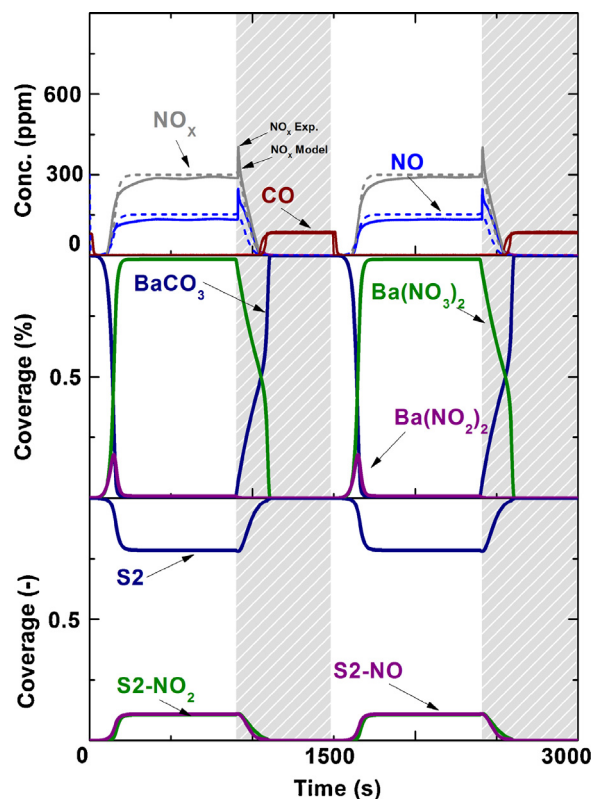
Fig. 2. 500 °C, Long NSR Cycle Performance. Upper panel: Measured (solid) and calculated (dashed) outlet NO_X, NO and CO concentrations during NSR cycles. NO_X desorption peak marked. Middle and lower panel: Calculated mean surface coverages. The catalyst (Cat. 1) was exposed to 300 ppm of NO, 10% O_2, 5% H_2O and 5% CO_2 during lean period (900 s) and to 375 ppm H_2, 625 ppm CO, 5% H_2O and 5% CO_2 during rich period (600 s) at 500 °C. Rich period is marked in gray.

CO as reducing agents. These regenerations steps are summarized in Table 3.

4. Results and discussion

4.1. Long cycles

Figs. 2–5 show the experimental and simulated results from the long NSR cycles with a 900-s long lean period and a 600-s long rich period over the 200 to 500 °C temperature range. The catalyst (Cat. 1) was exposed to 300 ppm of NO, 10% O_2, 5% H_2O and 5% CO_2 during the lean period and to 375 ppm H_2, 625 ppm CO, 5% H_2O and 5% CO_2 during the rich period. Fig. 2 shows the experimental and simulated results conducted at 500 °C, where the upper panel shows the experimental and calculated NO_X, NO and CO concentrations, and the lower panel shows the calculated mean coverages for Ba and S2 sites. The experimental and simulated results show a complete NO_X storage for about 45 s. The NO oxidation reaction during the storage period is important to be able to explain the different storage species correctly. The simulated level of NO reaches the experimental value according to the calculated thermodynamic equilibrium level for NO oxidation (cf. NO oxidation in Section 3.2). The calculated coverages presented in Fig. 1 show that NO_X is primarily stored as nitrates over Ba as $Ba(NO_3)_2$ in agreement with previous results by Lindholm et al. [21]. Similar results can be observed for the storage site S2, where NO_2 is the main storage species in the support, hence showing the importance of the NO oxidation reaction during the storage period. Furthermore, S2 is the main storage site at lower temperatures. Fridell et al. [44] previously showed that alumina is responsible for low temperature NO_X storage and, therefore, the parameters for the equilibrium constant for S2 are

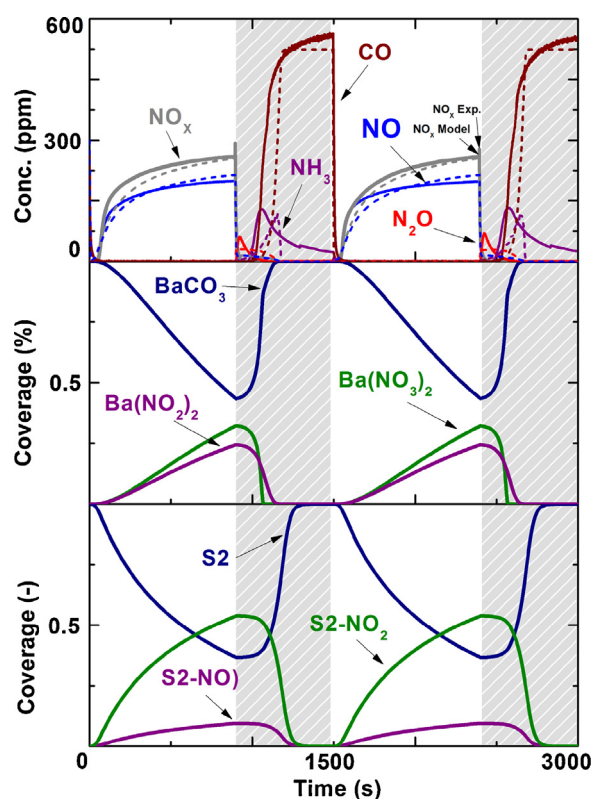**Fig. 3.** 400 °C, Long NSR Cycle Performance. Upper panel: Measured (solid) and calculated (dashed) outlet NO_X, NO and CO concentrations during NSR cycles. NO_X desorption peak marked. Middle and lower panel: Calculated mean surface coverages. The catalyst (Cat. 1) was exposed to 300 ppm of NO, 10% O_2, 5% H_2O and 5% CO_2 during lean period (900 s) and to 375 ppm H_2, 625 ppm CO, 5% H_2O and 5% CO_2 during rich period (600 s) at 400 °C. Rich period is marked in gray.

fitted for high storage capacity at low temperature. Since the temperature was 500 °C, this was apparent from the low calculated coverages for the S2 site in Fig. 2. Furthermore, the NO_X storage during the lean period showed a fast saturation where the NO_X slope after complete storage was high showing that there was only limited storage. As mentioned previously (cf. Section 3.4 NO_X storage), the shrinking-core rate expression was not used for barium particles. Due to the low site density of barium compared to S2, in combination with storage dominating total uptake, it was difficult to fit the diffusion resistance. However, we would like to highlight that this does not mean that barium does not have any diffusion resistance in the particle but is only a simplification. During the rich period, adsorbed NO_X is released from the storage sites and observed both in the experiment and simulation for about 10 s before reaching zero after the lean/rich switch. The CO breakthrough appears around 50 s into the rich period and reaches its equilibrium level about 50 s later due to the water gas shift reaction. The calculated CO reaches the equilibrium level about 10 s later than the experimental results. NH_3 and N_2O are not observed at this high temperature due to the fast NO_X release creating high local instantaneous NO_X/reductant ratios. Phil et al. [15] experimentally observed that high NO_X/reductant ratios favor N_2 over NH_3. Moreover, the NH_3–NO_X reaction at 500 °C is also very fast and any produced ammonia is most likely consumed within the catalyst monolith (cf. Table 2).

Fig. 3 shows the results for long NSR cycles conducted at 400 °C, where the experimental and calculated results show a complete NO_X storage for about 105 s. Similar to the results at higher temperature, NO_2 is the species mainly stored in the catalyst. Nitrites over Ba sites show an intense peak in the beginning of the lean period
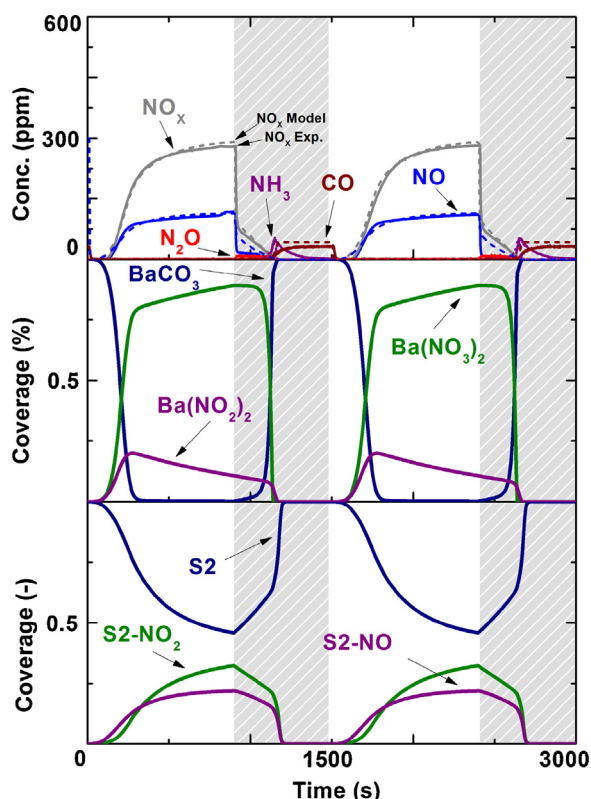
Fig. 4. 300 °C, Long NSR Cycle Performance. Upper panel: Measured (solid) and calculated (dashed) outlet NO_X, NO, N_2O, NH_3 and CO concentrations during NSR cycles. NO_X desorption peak marked. Middle and lower panel: Calculated mean surface coverages. The catalyst (Cat. 1) was exposed to 300 ppm of NO, 10% O_2, 5% H_2O and 5% CO_2 during lean period (900 s) and to 375 ppm H_2, 625 ppm CO, 5% H_2O and 5% CO_2 during rich period (600 s) at 300 °C. Rich period is marked in gray.

Fig. 5. 200 °C, Long NSR Cycle Performance. Upper panel: Measured (solid) and calculated (dashed) outlet NO_X, NO, N_2O, NH_3 and CO concentrations during NSR cycles. NO_X desorption peak marked. Middle and lower panel: Calculated mean surface coverages. The catalyst (Cat. 1) was exposed to 300 ppm of NO, 10% O_2, 5% H_2O and 5% CO_2 during lean period (900 s) and to 375 ppm H_2, 625 ppm CO, 5% H_2O and 5% CO_2 during rich period (600 s) at 200 °C. Rich period is marked in gray.

and are rapidly converted to nitrates, which was also the case in the detailed kinetic models by Olsson et al. [19,20] and Lindholm et al. [21]. Furthermore, the calculated coverages for S2 show higher storage capacity compared to that at 500 °C. The fraction of occupied S2 sites are still significantly lower than the Ba sites; however, the site density for S2 is about ten times higher than the Ba site density and hence, the total amount of NO_X stored over S2 is higher. As mentioned in the earlier section, S2 can be interpreted as alumina, ceria (when present) but possibly also sites related to barium because it has been suggested that different barium sites are available which are most likely to be the high temperature storage component. In addition, since S2 is a summary name for different components, no detailed reaction steps are proposed for this site. Also on this site, the adsorbed NO and NO_2 can be further oxidized to form nitrates, which is the dominating species at high temperatures [44]. However, in order to simplify the model, the reaction steps for the formation of nitrates have not been included. During the rich period, adsorbed NO_X is released and observed in the experiment and simulation for about 130 s from the storage sites after the lean/rich switch. The CO breakthrough appears directly after the NO_X levels decrease to zero during the rich period and reaches its equilibrium level about 50 s later due to the water gas shift reaction. However, similar to the results at 500 °C, the calculated CO reaches equilibrium about 10 s later than the experimental results because of its lower slope after the CO breakthrough. At this temperature, minor NH_3 production is observed both in the experiment and simulation (not marked in Fig. 3), which reaches a maximum of around 10 ppm during the rich period. The NO_X reduction using NH_3 is still relatively high compared to NH_3 production from adsorbed NO_X, hence a minor amount of ammonia

is observed. As previously mentioned, the NH_3-NO_X reaction is still fast at 400 °C and, therefore, the produced ammonia is most likely consumed thanks to the fast reduction. Small N_2O production is also observed experimentally and in the simulation (not shown in Fig. 3), although not at significant levels (max 2 ppm).

Figs. 4 and 5 show the results for long NSR cycles conducted at 300 and 200 °C, where the experimental and calculated results show a complete NO_X storage for about 130 and 55 s^^, respectively. The complete uptake time does not significantly increase for the experiments conducted at 300 compared to 400 °C. However, the slope of the NO_X concentration curve before reaching saturation during storage is lower than at higher temperatures, indicating higher NO_X storage capacity, which is also reflected in the calculated coverage of each site. During NO_X storage at 200 °C, the complete NO_X uptake time is only about 55 s; however, the slope after the NO_X breakthrough is lower compared to the results at 300 °C, resulting in higher NO_X storage capacity. Furthermore, at 300 °C, stored nitrites over Ba sites are more stable compared to storage at higher temperatures and reach maxima around 25% before slowly decreasing towards the end of the lean cycle while corresponding nitrates are formed. However, at 200 °C, due to its thermodynamic equilibrium, the storage capacity of nitrites is stable and does not reach any maxima during the lean period. The storage of NO over the S2 sites at 300 °C are thermodynamically more stable compared to higher temperatures and continues to increase during the lean period. Furthermore, the effect of the shrinking-core model is clearly observed at these low temperatures (300 and 200 °C). Specifically, the NO_X slope after complete adsorption is very low and reaches saturation more slowly compared to higher temperatures and is reflected in the calculated S2 coverage

Table 4
Site density and geometric surface area (GSA) for Cat. 1 and Cat. 2.

Cat.Nr	Ba (x 10^{-5})[a]	S2(x 10^{-5})[a]	Ce(x 10^{-5})[a]	S3(x 10^{-5})[a]	GSA[b]
1	63	838	2617	-	3346
2	63	727	-	1974	2444

[a] $-mol/m^2$
[b] $- m^2/m^3$

slopes. This feature is incorporated in the model and explained by the increasing diffusion resistance when NO_X is stored further into the particles. During the rich period, NO_X release is observed but no significant NO_X peak is detected, indicating a slower regeneration rate at 300 °C. The NO_X levels reach zero around 150 s into the rich period before an ammonia peak is observed both experimentally and in the simulation. Before the NH_3 peak, a small amount of N_2O is observed and it is possible that the NH_3 produced is oxidized to N_2O due to a reaction between NH_3 and stored NO_X. The results show that when the amount of stored NO_X becomes low, the consumption rate of the NH_3 produced is likewise low, hence ammonia is observed. During the NSR cycles at 200 °C, no NO_X peak is observed when switching over to the rich period. Furthermore, the NO_X level reaches zero directly during the rich period. The experimental and calculated results show strong N_2O and NH_3 production during the rich period. As previously mentioned, since no NO_X is present in the inlet feed gas, NH_3 is produced from stored NO_X, hence the

slow regeneration of stored NO_X at low temperatures enhances NH_3 production. However, the NH_3 breakthrough is delayed about 100 s into the rich period, possibly because it is being oxidized by nitrates in the beginning of the rich period, when the amount of stored NO_X is high, as previously discussed for the NSR cycle at 300 °C. The results from the fitted parameters are presented in Tables 4–7.

4.2. Short cycles

The kinetic parameters in the model were fitted to long NSR cycles and thereafter validated by using short NSR cycles that are closer to real applications. All fitted parameters were unchanged when the model was validated using short NSR cycles. Figs. 6–9 show the experimental and simulated results from the short NSR cycles with a 60 s lean period and a 5 s rich period over the 200 to 500 °C temperature range. Catalyst (Cat. 1) was exposed to 300 ppm

Table 5
Kinetic parameters for NO oxidation, water gas shift reaction, NO_X adsorption and desorption over barium and S2 and oxygen storage over ceria and S3.

No.	Reaction rate	Pre-exponential factor	Activation energy (kJ/mol)	Change in S (%) at 300^0C	Change in S (%) at 500^0C
1	$r_1 = k_1 C_{O_2}^{0.5} C_{NO} \quad -\dfrac{k_1}{K_{eq.1}} C_{NO_2}$	$5.0 \times 10^{3\,g}$	42	Pre-exp: 0.21 Act.En: 0.87	Pre-exp: 0.77 Act.En: 1.94
2	$r_2 = k_3 C_{H_2O} C_{CO} \quad -\dfrac{k_3}{K_{eq.2}} C_{CO_2} C_{H_2}$	$2 \times 10^{7\,g}$	76	Pre-exp: 3.17 Act.En: 13.0	Pre-exp: 0.22 Act.En: 0.86
3[a]	$r_3 = k_5 C_{NO_2} C_{O_2}^{1/4} \theta_{BaCO_3} \quad -\dfrac{k_5}{K_{eq.3}} C_{CO_2}^{1/2} \theta_{Ba(NO_3)_2}$	$2 \times 10^{7\,h}$	75	Pre-exp: 0.91 Act.En: 3.29	Pre-exp: 2.60 Act.En: 8.85
4[b]	$r_4 = k_7 C_{NO} \quad C_{O_2}^{1/4} \theta_{BaCO_3} \quad -\dfrac{k_7}{K_{eq.4}} C_{CO_2}^{1/2} \theta_{Ba(NO_2)_2}$	$1 \times 10^{7\,h}$	80	Pre-exp: 0.34 Act.En: 1.38	Pre-exp: 0.44 Act.En: 1.40
5[c,d,e]	$r_5 = k_9 C_{NO_2} \theta_{S2} - \dfrac{k_9}{K_{eq.5}} \theta_{S2NO_2}$	Cat.1: $6 \times 10^{2\,h}$ Cat.2 : $6 \times 10^{3\,h}$	20	Pre-exp: 0.98 Act.En: 1.93	Pre-exp: 0.59 Act.En: 1.10
6[c,d,f]	$r_6 = k_{11} C_{NO} \quad \theta_{S2} - \dfrac{k_{11}}{K_{eq.6}} \theta_{S2NO}$	Cat.1: $6 \times 10^{2\,h}$ Cat.2 : $6 \times 10^{3\,h}$	20	Pre-exp: 0.88 Act.En: 1.66	Pre-exp: 0.70 Act.En: 1.21
7	$r_7 = k_7 C_{O_2} \theta_{CeO_{1.5}}$	$1 \times 10^{2\,h}$	40	Pre-exp: 0.44 Act.En: 0.10	Pre-exp: 0.19 Act.En: 0.28
8	$r_8 = k_8 C_{O_2} \theta_{S3}$	$1 \times 10^{2\,h}$	40	Pre-exp: 0.44 Act.En: 0.10	Pre-exp: 0.19 Act.En: 0.28

[a] $- \Delta H$ = -113.9 kJ/mol [20] and ΔS= -60 J/mol K
[b] $-\Delta H$ = -63.75 kJ/mol [20] and ΔS= -25 J/mol K
[c] $-\Delta H$ = -52 kJ/mol and ΔS= -20 J/mol K

[d] $- \alpha = \alpha_1 e^{\frac{-\beta_1}{RT}}$,   where α_1 for Cat.1 = 1×10^6 m^2/s and β_1 for Cat.1 = 70 kJ/mol
where α_1 for Cat.2 = 5.5×10^5 m^2/s and β_1 for Cat.2 = 22 kJ/mol

[e] –Change in S_{r5} (%),   at 300^0C for α_1 is 5.14 and for β_1 is 19.6
at 500^0C for α_1 is 0.50 and for β_1 is 1.34

[f] – Change in S_{r6} (%),   at 300^0C for α_1 is 5.04 and for β_1 is 19.2
at 500^0C for α_1 is 0.40 and for β_1 is 1.60

[g] – Pre-exponential factor units: kmol/(s m^3)

[h] – Pre-exponential factor units: 1/(s m)

Table 6
Kinetic parameters for NH_3 production and reduction and N_2O production.

No. [a]	Reaction rate	Pre-exponential factor	Activation energy (kJ/mol)	Change in S (%) at 300^0C	Change in S (%) at 500^0C
9	$r_9 = k_9 C_{CO_2} C_{H_2} \theta_{Ba(NO_3)_2}$	Cat.1: 1×10^4 Cat.2: 3×10^3	20	Pre-exp: 0.30 Act.En: 0.60	Pre-exp: 0.26 Act.En: 0.45
10	$r_{10} = k_{10} C_{CO_2} C_{H_2} \theta_{Ba(NO_2)_2}$	Cat.1: 1×10^4 Cat.2: 3×10^3	20	Pre-exp: 0.30 Act.En: 0.60	Pre-exp: 0.26 Act.En: 0.45
11	$r_{11} = k_{11} C_{H_2} \theta_{S2-NO_2}$	Cat.1: 1×10^4 Cat.2: 3×10^3	20	Pre-exp: 0.30 Act.En: 0.60	Pre-exp: 0.26 Act.En: 0.45
12	$r_{12} = k_{12} C_{H_2} \theta_{S2-NO}$	Cat.1: 1×10^4 Cat.2: 3×10^3	20	Pre-exp: 0.30 Act.En: 0.60	Pre-exp: 0.26 Act.En: 0.45
13	$r_{13} = k_{13} C_{NH_3} C_{CO_2} \theta_{Ba(NO_3)_2}$	Cat.1: 3×10^4 Cat.2: 4.9×10^5	Cat.1: 42 Cat.2: 53	Pre-exp: 0.56 Act.En: 1.23	Pre-exp: 0.21 Act.En: 0.64
14	$r_{14} = k_{14} C_{NH_3} C_{CO_2} \theta_{Ba(NO_2)_2}$	Cat.1: 3×10^4 Cat.2: 4.9×10^5	Cat.1: 42 Cat.2: 53	Pre-exp: 0.33 Act.En: 0.92	Pre-exp: 0.09 Act.En: 0.16
15	$r_{15} = k_{15} C_{NH_3} C_{H_2} \theta_{S2-NO_2}$	Cat.1: 3×10^4 Cat.2: 4.9×10^5	Cat.1: 42 Cat.2: 53	Pre-exp: 0.69 Act.En: 2.54	Pre-exp: 0.17 Act.En: 0.27
16	$r_{16} = k_{16} C_{NH_3} \theta_{S2-NO}$	Cat.1: 3×10^4 Cat.2: 4.9×10^5	Cat.1: 42 Cat.2: 53	Pre-exp: 0.86 Act.En: 2.99	Pre-exp: 0.15 Act.En: 0.24
17	$r_{17} = k_{17} C_{CO_2} C_{NH_3} \theta_{Ba(NO_3)_2}$	Cat.1: 1×10^1 Cat.2: 2×10^1	10	Pre-exp: 0.16 Act.En: 0.40	Pre-exp: 0.02 Act.En: 0.01
18	$r_{18} = k_{18} C_{CO_2} C_{NH_3} \theta_{Ba(NO_2)_2}$	Cat.1: 1×10^1 Cat.2: 2×10^1	10	Pre-exp: 0.16 Act.En: 0.40	Pre-exp: 0.02 Act.En: 0.01
19	$r_{19} = k_{19} C_{NH_3} \theta_{S2-NO_2}$	Cat.1: 1×10^1 Cat.2: 2×10^1	10	Pre-exp: 0.16 Act.En: 0.40	Pre-exp: 0.02 Act.En: 0.01
20	$r_{20} = k_{20} C_{NH_3} \theta_{S2-NO}$	Cat.1: 1×10^1 Cat.2: 2×10^1	10	Pre-exp: 0.16 Act.En: 0.40	Pre-exp: 0.02 Act.En: 0.01

[a]– Pre-exponential factor units: 1/(s m)

Table 7
Kinetic parameters for regeneration of barium, S2 and ceria.

| No.	Reaction rate	Pre-exponential factor	Activation energy (kJ/mol)	Change in S (%) at 300^0C	Change in S (%) at 500^0C
21[a]	$r_{21} = k_{21} C_{CO_2} C_{H_2} \theta_{Ba(NO_3)_2}$	2×10^2	30	Pre-exp: 0.66 Act.En: 1.66	Pre-exp: 0.11 Act.En: 0.11
22[a]	$r_{22} = k_{22} C_{CO} \, \theta_{Ba(NO_3)_2}$	2×10^2	30	Pre-exp: 0.66 Act.En: 1.66	Pre-exp: 0.11 Act.En: 0.11
23[a]	$r_{23} = k_{23} C_{CO_2} C_{H_2} \theta_{Ba(NO_2)_2}$	2×10^2	30	Pre-exp: 0.55 Act.En: 1.30	Pre-exp: 0.11 Act.En: 0.13
24[a]	$r_{24} = k_{24} C_{CO} \, \theta_{Ba(NO_2)_2}$	2×10^2	30	Pre-exp: 0.55 Act.En: 1.30	Pre-exp: 0.11 Act.En: 0.13
25[a]	$r_{25} = k_{25} C_{H_2} \theta_{S2-NO_2}$	2×10^2	30	Pre-exp: 0.26 Act.En: 0.46	Pre-exp: 0.06 Act.En: 0.12
26[a]	$r_{26} = k_{26} C_{CO} \theta_{S2-NO_2}$	2×10^2	30	Pre-exp: 0.26 Act.En: 0.46	Pre-exp: 0.06 Act.En: 0.12
27[a]	$r_{27} = k_{27} C_{H_2} \theta_{S2-NO}$	2×10^2	30	Pre-exp: 0.18 Act.En: 0.27	Pre-exp: 0.11 Act.En: 0.08
28[a]	$r_{28} = k_{28} C_{CO} \theta_{S2-NO}$	2×10^2	30	Pre-exp: 0.18 Act.En: 0.27	Pre-exp: 0.11 Act.En: 0.08
29[a]	$r_{29} = k_{29} C_{CO} \theta_{CeO_2}$	5×10^4	35	Pre-exp: 0.81 Act.En: 2.17	Pre-exp: 0.13 Act.En: 0.33
30[a]	$r_{30} = k_{30} C_{H_2} \theta_{CeO_2}$	1×10^4	25	Pre-exp: 0.51 Act.En: 1.1	Pre-exp: 0.08 Act.En: 0.15
31[a]	$r_{31} = k_{31} C_{H_2} \theta_{S3-O}$	1×10^4	25	Pre-exp: 0.51 Act.En: 1.1	Pre-exp: 0.08 Act.En: 0.15
32[a]	$r_{32} = k_{32} C_{CO} \theta_{S3-O}$	5×10^4	35	Pre-exp: 0.81 Act.En: 2.17	Pre-exp: 0.13 Act.En: 0.33
33[b]	$r_{33} = k_{33} C_{NO} C_{H_2}$	1×10^2	60	Pre-exp: 0.19 Act.En: 0.19	Pre-exp: 0.27 Act.En: 0.18
34[b]	$r_{34} = k_{34} C_{NO} C_{CO}$	1×10^2	60	Pre-exp: 0.26 Act.En: 0.41	Pre-exp: 0.24 Act.En: 0.23

[a]– Pre-exponential factor units: 1/(s m)

[b]– Pre-exponential factor units: $kmol/(s \, m^3)$
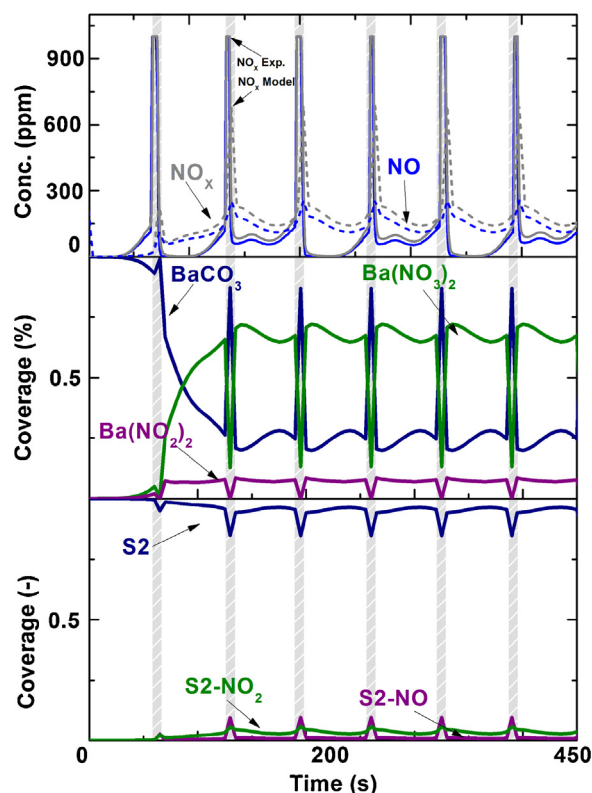
Fig. 6. 500 °C, Short NSR Cycle Performance. Upper panel: Measured (solid) and calculated (dashed) outlet NO_X, and NO concentrations during NSR cycles. NO_X desorption peak marked. Middle and lower panel: Calculated mean surface coverages. The catalyst (Cat. 1) was exposed to 300 ppm of NO, 10% O_2, 5% H_2O and 5% CO_2 during lean period (60 s) and to 2700 ppm H_2, 5% H_2O and 5% CO_2 during rich period (5 s) at 500 °C. Rich period is marked in gray.

Fig. 7. 400 °C, Short NSR Cycle Performance. Upper panel: Measured (solid) and calculated (dashed) outlet NO_X, and NO concentrations during NSR cycles. NO_X desorption peak marked. Middle and lower panel: Calculated mean surface coverages. The catalyst (Cat. 1) was exposed to 300 ppm of NO, 10% O_2, 5% H_2O and 5% CO_2 during lean period (60 s) and to 2700 ppm H_2, 5% H_2O and 5% CO_2 during rich period (5 s) at 400 °C. Rich period is marked in gray.

of NO, 10% O_2, 5% H_2O and 5% CO_2 during the lean period and to 2700 ppm H_2, 4500 ppm CO, 5% H_2O and 5% CO_2 during the rich period. For all short NSR experiments, the results showed strong NO_X desorption after the switch to the rich period during the first cycles until the storage reached steady-state. However, our simulation showed lower NO_X desorption than the experiment. The NH_3 produced reacted with stored NO_x and this reaction was likely too fast for the initial cycles of the model, resulting in low NO_X and NH_3 peaks. Fig. 6 shows the experimental and simulated results conducted at 500 °C, where the upper panel shows the experimental and calculated NO_X, NO and CO concentrations, whereas the lower panel shows the calculated mean coverages for Ba and S2 sites. Both the experimental and simulated NO_X storage shows a complete storage at the beginning of the first lean period. The lean-phase NOx maxima is likely due to heat waves. As Epling et al. [52] observed previously on the same catalyst, Cat. 1 can have a temperature maxima in lean phase due to slow dissipation via conduction of exotherms generated during rich and rich/lean transition. As Epling et al. [52] pointed out, at high temperatures such as 500 °C in Fig. 6, the lean-phase NOx storage is controlled by the thermodynamics. Therefore, even a slight increase in reaction temperature can shift the maximum NOx storage capacity resulting in the desorption of NOx. As previously mentioned, no heat balances are solved in the simulations due to the relatively small temperature gradients for the long NSR cycles. However, for the validation experiments, the short NSR cycles shows higher temperature gradients, which may be the main reason for the slight difference between the experimental results and simulations and also why the model do not predict a NOx maxima in lean period.

The model can predict the gradual decrease in storage capacity until it reaches its stored species equilibrium level, which can be
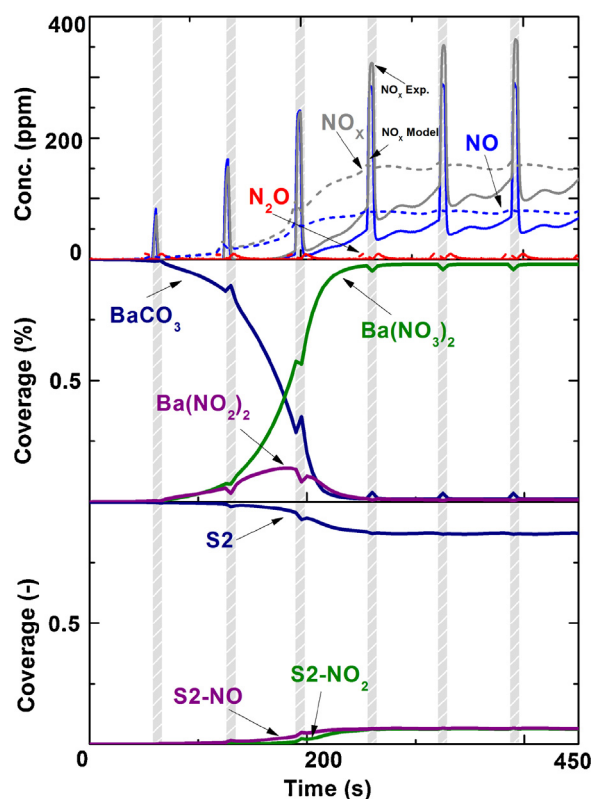
observed in the calculated coverages. Similar to the long NSR cycles, no NH_3 or N_2O was observed during the rich period at such a high temperature.

Fig. 7 shows the experimental and simulated results conducted at 400 °C. Similar to the previous temperature, the model is capable of predicting a gradual decrease in storage capacity until reaching its equilibrium level of the stored species. Furthermore, a small N_2O peak was observed in the experimental and simulated results. Directly after the switch to the rich period, an N_2O peak (10 ppm) was observed in the simulation. However, the experimental peaks have a 10-s delay and were observed just as the lean period started. Furthermore, the long NSR cycles at 400 °C did not show any N_2O peak as shown in the short cycle. The reason for the N_2O production might be the high H_2 concentration for the short cycles, which enhances the NH_3 production and thereby the formation of N_2O by the reduction of stored NO_x with NH_3.

Figs. 8 and 9 show the experimental and simulated results conducted at 300 and 200 °C, respectively. As previously observed, the model is able to predict the gradual decrease in storage capacity after repeated cycles, which also was the case at higher temperatures. The model shows a slightly lower regeneration capacity compared to the experiments and cannot predict the total experimental NO_X uptake at the beginning of each cycle. The regeneration at 200 °C is higher and the model is capable of predicting the total NO_X uptake better than the cycles performed at 300 °C. Furthermore, the gradual decrease in storage observed both during experiments and simulation is also reflected in calculated coverages. At 300 and 200 °C, although the coverage of the different species do not reach their steady-state level during NSR cycling, they seem to go towards steady state, which is similar to the calculated coverage for the long NSR cycles. Moreover, in both
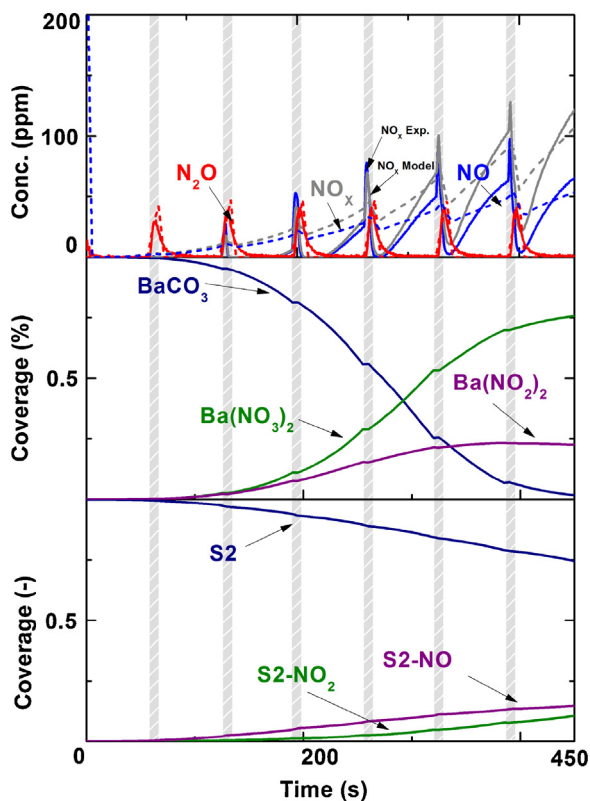
Fig. 8. 300 °C, Short NSR Cycle Performance. Upper panel: Measured (solid) and calculated (dashed) outlet NO_X, and NO concentrations during NSR cycles. NO_X desorption peak marked. Middle and lower panel: Calculated mean surface coverages. The catalyst (Cat. 1) was exposed to 300 ppm of NO, 10% O_2, 5% H_2O and 5% CO_2 during lean period (60 s) and to 2700 ppm H_2, 5% H_2O and 5% CO_2 during rich period (5 s) at 300 °C. Rich period is marked in gray.
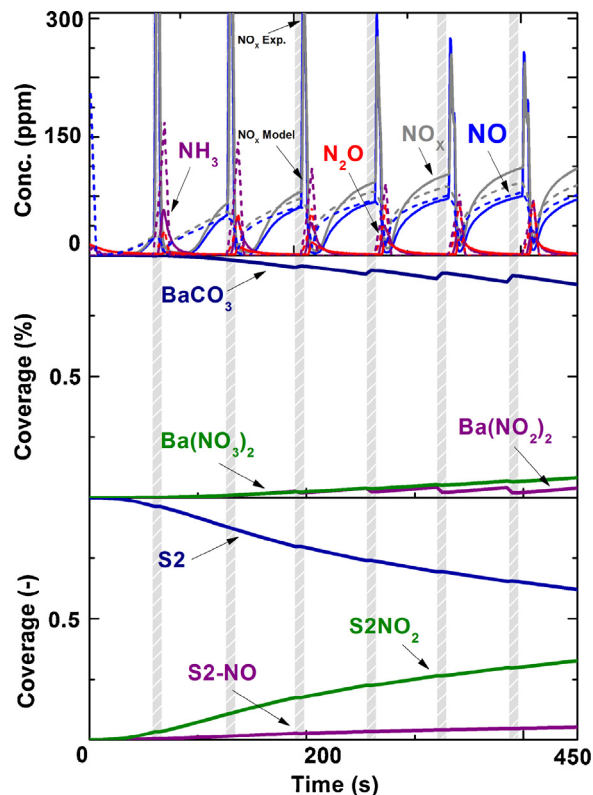
Fig. 9. 200 °C, Short NSR Cycle Performance. Upper panel: Measured (solid) and calculated (dashed) outlet NO_X, and NO concentrations during NSR cycles. NO_X desorption peak marked. Middle and lower panel: Calculated mean surface coverages. The catalyst (Cat. 1) was exposed to 300 ppm of NO, 10% O_2, 5% H_2O and 5% CO_2 during lean period (60 s) and to 2700 ppm H_2, 5% H_2O and 5% CO_2 during rich period (5 s) at 200 °C. Rich period is marked in gray.
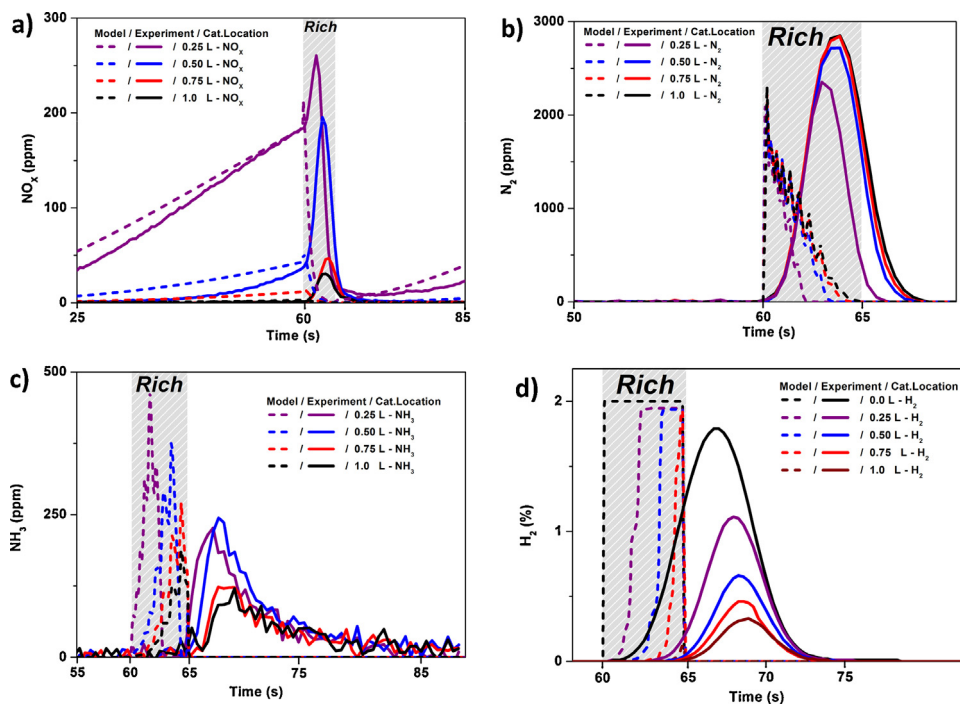
Fig. 10. Species transient at different location through the catalyst during NSR cycle. Measured (solid) and calculated (dashed). The catalyst was exposed to 300 ppm of NO, 10% O_2, 5% H_2O and 5% CO_2 during lean period (60 s) and to 2% H_2, 5% H_2O and 5% CO_2 during rich period (5 s) at 325 °C. Rich period is marked in gray. Note the magnification of the rich phase in b), c) and d).

Figs. 8 and 9, a large N_2O peak can be seen in both the experimental and simulated results. Although no NH_3 peak was observed in either the experiments or the simulations at 300 °C, strong NH_3 production can be observed both experimentally and in the model at 200 °C (see Fig. 9). The calculated NH_3 production is higher than the experimental result for the initial cycles, but reaches the same level as the experiments in later cycles.

4.3. Simulations of spatial resolved measurements

The developed model was validated by using SpaciMS experiments performed over another LNT catalyst (Cat. 2, cf. Experiments). Most parameters fitted for Cat. 1 were used for validating the intra-catalyst simulation using Cat. 2. However, some of the parameters had to be re-fitted due to the different material properties of Cat. 2. The re-tuned parameters for Cat. 2 are presented along with remaining parameters for Cat. 1 in Tables 4–7. The density of the S2 storage site and the diffusion rates for the S2 (α and β) support material were changed due to varying support materials. Furthermore, since oxygen was stored over another site in Cat. 2 (cf. Section 3.5 oxygen storage over ceria, S3 and Table 1), the S3 site density was fitted to the simulations. Finally, the NH_3 reduction rates were slightly decreased during the rich period for Cat. 2. Fig. 10a shows the experimental and simulated intra-catalyst NO_X storage profile. The experiments and simulations show a complete NO_X uptake during the lean cycle when studying the outlet concentration (at 1.0 L in Fig. 10 a). The validation simulation well predicted the experimental lean-phase NO_X profile where it could be observed that most of the inlet NO_X was stored in the first half of the catalyst. Furthermore, Fig. 10b shows the produced rich-phase N_2 transients along the catalyst. The results show that most of the nitrogen was produced in the first half of the catalyst; this agrees well with the NO_X storage distribution which was the source of N_2 during regeneration. Notably in assessing Fig. 10b–d, the measurements contain temporal broadening of the square regeneration pulse that is not contained in the model. The salient feature in comparing the experimental and numerical results of Fig. 10b is that both have a common leading edge, and similar relative temporal separation between the pulse tails for steps between the various intra-catalyst locations. This common leading edge and progressively delayed tails is generally characteristic of the spatiotemporal nature of inert products [18]. Furthermore, the experiments in Fig. 10c showed a high NH_3 production in the first part of the catalyst. Partridge et al. [18] denoted the large ammonia production in the "buildup region" in the catalyst front which moved along the catalyst axis in a "plug flow" behavior. The ammonia produced was thereafter used for an LNT regeneration reaction in the latter part of the catalyst. Pihl et al. [17] showed that most of the ammonia was produced in the first half of the catalyst and was reduced along the catalyst, with the remaining stored NO_X forming byproducts, such as N_2O, during regeneration in the rich period. Results from the kinetic model showed an ammonia maximum in the first quarter of the catalyst, which started to decrease along the axis. As previously mentioned (cf. Section 3.5 oxygen storage over ceria and S3), the oxygen storage material must be accounted for in the Cat. 2 model. Simulations without the oxygen storage material showed an excess of available hydrogen, which resulted in an over-predicted ammonia production; hence, accounting for the oxygen storage material in the Cat. 2 model was necessary to accurately predict NH_3 production. This can be further examined in Fig. 10d, where the high concentration of hydrogen from the simulations is continuously being reduced along the catalyst axis, partially due to a reduction of NO_X, but mainly from reacting with stored oxygen. The salient feature in comparing the experimental and numerical results of Fig. 10d is that both have similar progressive delay in the leading edge between the various intra-catalyst locations, and

a common tailing edge; this is generally characteristic of the spatiotemporal nature of reductants, and the reductant nature of NH_3 is similarly apparent in Fig. 10c [18]. Although the SpaciMS experiments did not measure N_2O, the simulations showed increased N_2O production with decreasing concentrations of NH_3 (not shown in the figures), further indicating that the NO_X reduction with ammonia generates N_2O as a product along the catalyst length. The results are consistent with the study by Pihl et al. [17], which suggested that NH_3 may be oxidized by stored NO_X and oxygen along the catalyst axis. Partridge et al. [18] also suggested that the produced NH_3 might also be oxidized by stored oxygen. The model well predicts the NH_3 profile along the catalyst axis without including any NH_3 oxidation by surface oxygen steps. It cannot, however, be excluded that NH_3 oxidation by stored oxygen does not play a part in the NH_3 conversion. Nevertheless, to keep the model as simple as possible, NH_3 oxidation by stored oxygen was not included and was also not essential to accurately predicting the NH_3 reduction. The predicted NH_3 concentrations during the simulations of the long and short cycles together with the validation calculations indicate that the NO_X reduction with NH_3 is the main pathway for the decreased ammonia along the catalyst axis. This result is consistent with recent findings by Choi et al. [51], where they proposed that the N_2O was mainly formed by produced NH_3 and stored NO_X along the catalyst.

5. Sensitivity analysis

The results from the sensitivity analysis are shown in Tables 5–7. These show that the parameters for the diffusion rate are very important compared to other parameters during the lean period for the storage site S2 ($r_5–r_6$ in Table 5), especially during the low temperature NSR cycles where the storage site S2 is most active; the activation energy for the S2 sites is significant as well. This is also observed when the model is validated with SpaciMS measurements where the parameters mentioned above had to be changed for Cat. 2.

During the rich period, the sensitivity analysis indicates that parameters for the regeneration of S2 site using NH_3 (NH_3-SCR chemistry, $r_{15}–r_{16}$) in Table 6 are very important, especially during low temperature NSR, which show the highest relative sensitivity. The significances of the parameters are again observed when the model is validated with SpaciMS measurements where the corresponding parameters had to be changed, indicating the relative importance of the NH_3-SCR reaction during the regeneration period. Furthermore, during the rich period direct regeneration of Ba and oxygen storage site (Ce for Cat. 1 or S3 for Cat. 2), $r_{21}–r_{24}$ and $r_{29}–r_{32}$ respectively, using H_2 or CO shows a relatively high sensitivity compared to the direct regeneration of S2 $r_{25}–r_{28}$, shown in Table 7. Due to the larger NO_X storage capacity of S2, the regeneration of S2 is more sensitive to the NH_3-SCR chemistry than direct regeneration using H_2 or CO, especially during low temperature NSR as discussed previously.

6. Concluding remarks

The objective of the present study was to investigate the mechanisms of NH_3 and N_2O formation for NO_X storage and reduction catalysts. The model was developed and fitted using long NSR cycles and was later validated against shorter and more realistic NSR cycles while keeping the parameters unchanged. To verify the intra-catalyst storage and reduction, the model was further validated against intra-catalyst measurements of a different catalyst focusing on the formation and consumption of ammonia.

The global NSR model was developed using subsystems, where the first subsystem described NO oxidation and water–gas shift

reaction. The second subsystem described the storage of NO_X and oxygen in the catalyst. Finally, the last subsystem described the regeneration of the catalyst during the rich period, where the formation of NH_3 and N_2O as byproducts from the reduction of NO_X was included. Two different catalysts, denoted by Catalyst 1 and Catalyst 2, were used in the model. The experiments performed with the first catalyst were used in the model development for tuning the parameters during long NSR cycles and were validated during short NSR cycles, while the second catalyst was used for validating intra-catalyst concentrations. However, due to some differences in the catalytic material, some parameters had to be re-fitted for the second catalyst.

During the lean period, NO_X was stored on barium (Ba) and the support material (S2) for both catalysts. Oxygen was stored on the support material (CeO_2) for Cat. 1. The second catalyst, Cat. 2, did not contain any ceria. However, it became necessary to add an oxygen storage site for Cat. 2 and, therefore, an oxygen storage site (S3) was included, which might be the noble metal sites. During the rich period, NO_X was reduced by H_2 and CO, producing nitrogen and ammonia. NH_3 is assumed to further react with stored NO_X forming N_2O. This step was necessary to simulate the N_2O peak before the NH_3 breakthrough during the rich period.

Pihl et al. [17] and Partridge et al. [18] discussed the need for a kinetic model to predict the formation of NH_3 and N_2O during rich cycles to better understand the NSR catalyst for future catalyst development and design. The model describes the NO_X storage and reduction experiments adequately for both long and short cycles. The simulations accurately predicted the NH_3 production during the rich period, as well as the formation of N_2O from stored NO_X. It became necessary to include the formation of N_2O from NH_3 and stored NO_X to describe the production of NH_3 and N_2O during the rich period. The simulations were consistent with the regeneration scheme of the catalyst during the rich period proposed by Pihl et al. [17], where it was suggested that NH_3 was mostly produced in the front and consumed along the catalyst. The model shows that most NO_X is stored in the catalyst front, which results in a high production of NH_3 in the beginning of the sample, which agrees well with the SpaciMS measurements. The simulation showed that ammonia reacted further along the catalyst with the remaining stored NO_X to form N_2O.

Acknowledgments

References

[1] N. Takahashi, H. Shinjoh, T. Iijima, T. Suzuki, K. Yamazaki, K. Yokota, H. Suzuki, N. Miyoshi, S.-i. Matsumoto, T. Tanizawa, T. Tanaka, S.-s. Tateishi, K. Kasahara, Catal. Today 27 (1996) 63–69.

[2] H. Abdulhamid, E. Fridell, M. Skoglundh, Appl. Catal. B: Environ. 62 (2006) 319–328.

[3] I. Nova, L. Lietti, L. Castoldi, E. Tronconi, P. Forzatti, J. Catal. 239 (2006) 244–254.

[4] P. Kočí, Š. Bártová, D. Mráček, M. Marek, J.-S. Choi, M.-Y. Kim, J. Pihl, W. Partridge, Top. Catal 56 (2013) 118–124.

[5] L. Castoldi, I. Nova, L. Lietti, P. Forzatti, Catal. Today 96 (2004) 43–52.

[6] I. Nova, L. Castoldi, L. Lietti, E. Tronconi, P. Forzatti, Top. Catal. 42-43 (2007) 21–25.

[7] L. Cumaranatunge, S.S. Mulla, A. Yezerets, N.W. Currier, W.N. Delgass, F.H. Ribeiro, J. Catal. 246 (2007) 29–34.

[8] S.S. Mulla, S.S. Chaugule, A. Yezerets, N.W. Currier, W.N. Delgass, F.H. Ribeiro, Catal. Today 136 (2008) 136–145.

[9] J.-S. Choi, W.P. Partridge, J.A. Pihl, C.S. Daw, Catal. Today 136 (2008) 173–182.

[10] I. Nova, L. Lietti, P. Forzatti, Catal. Today 136 (2008) 128–135.

[11] L. Lietti, I. Nova, P. Forzatti, J. Catal. 257 (2008) 270–282.

[12] R.D. Clayton, M.P. Harold, V. Balakotaiah, Appl. Catal. B: Environ. 84 (2008) 616–630.

[13] M.M. Baum, E.S. Kiyomiya, S. Kumar, A.M. Lappas, V.A. Kapinus, H.C. Lord Iii, Environ. Sci. Technol. 35 (2001) 3735–3741.

[14] J.H. Seinfeld, S.N. Pandis, Atmospheric Chemistry and Physics: From Air Pollution To Climate Change, John Wiley & Sons, New York, 1998.

[15] Overview of Greenhouse Gases, United States Environmental Protection Agency, Washington, DC, Accessed Date: 2013-10-04, http://epa.gov/climatechange/ghgemissions/gases/n2o.html

[16] T. Szailer, J.H. Kwak, D.H. Kim, J.C. Hanson, C.H.F. Peden, J. Szanyi, J. Catal. 239 (2006) 51–64.

[17] J.A. Pihl, J.E., Parks, C.S., Daw, T.W. Root, Product Selectivity During Regeneration of Lean NO_X Trap Catalysts, SAE Technical Paper 2006-01-3441, 2006.

[18] W.P. Partridge, J.S. Choi, Appl. Catal. B–Environ. 91 (2009) 144–151.

[19] L. Olsson, D. Monroe, R.J. Blint, Ind. Eng. Chem. Res. 45 (2006) 8883–8890.

[20] L. Olsson, R.J. Blint, E. Fridell, Ind. Eng. Chem. Res. 44 (2005) 3021–3032.

[21] A. Lindholm, N.W. Currier, J.H. Li, A. Yezerets, L. Olsson, J. Catal. 258 (2008) 273–288.

[22] U. Tuttlies, V. Schmeißer, G. Eigenberger, Chem. Eng. Sci. 59 (2004) 4731–4738.

[23] L. Olsson, H. Persson, E. Fridell, M. Skoglundh, B. Andersson, J. Phys. Chem. B 105 (2001) 6895–6906.

[24] P. Koci, F. Plat, J. Stepanek, S. Bartova, M. Marek, M. Kubicek, V. Schmeisser, D. Chatterjee, M. Weibel, Catal. Today 147 (2009) S257–S264.

[25] L. Olsson, M. Fredriksson, R.J. Blint, Appl. Catal. B: Environ. 100 (2010) 31–41.

[26] J. Xu, M.P. Harold, V. Balakotaiah, Appl. Catal. B: Environ. 104 (2011) 305–315.

[27] D. Bhatia, M.P. Harold, V. Balakotaiah, Catal. Today 151 (2010) 314–329.

[28] D. Bhatia, R.D. Clayton, M.P. Harold, V. Balakotaiah, Catal. Today 147 (2009) S250–S256, Supplement.

[29] J. Hepburn, T., Kenney, E. Thanasiu, SAE Technical Paper 982596, 1998.

[30] AVL BOOST Aftertreatment manual, AVL, http://www.avl.com, 2011.

[31] S. Shwan, J. Jansson, J. Korsgren, L. Olsson, M. Skoglundh, Catal. Today 197 (2012) 24–37.

[32] S. Shwan, R. Nedyalkova, J. Jansson, J. Korsgren, L. Olsson, M. Skoglundh, Top. Catal. 56 (2013) 80–88.

[33] J.R. Welty, C.E. Wicks, R.E. Wilson, G. Rorrer, Fundamentals of Momentum, Heat, and Mass Transfer, John Wiley & Sons, Inc., USA, 2001.

[34] S. Erkfeldt, E. Jobson, M. Larsson, Top. Catal. 16-17 (2001) 127–131.

[35] C. Ratnasamy, J.P. Wagner, Catal. Rev. 51 (2009) 325–440.

[36] P. Koci, M. Schejbal, J. Trdlicka, T. Gregor, M. Kubicek, M. Marek, Catal. Today 119 (2007) 64–72.

[37] I. Toftefors, The water–gas shift reaction in catalytic exhaust gas aftertreatment sytems, Master of Science Report, Department of Chemical and Biological Engineering, Chalmers University of Technology, Gothenburg, 2009.

[38] H. Mahzoul, J.F. Brilhac, P. Gilot, Appl. Catal. B: Environ. 20 (1999) 47–55.

[39] W.S. Epling, J.E. Parks, G.C. Campbell, A. Yezerets, N.W. Currier, L.E. Campbell, Catal. Today 96 (2004) 21–30.

[40] D. James, E. Fourré, M. Ishii, M. Bowker, Appl. Catal. B: Environ. 45 (2003) 147–159.

[41] L. Lietti, P. Forzatti, I. Nova, E. Tronconi, J. Catal. 204 (2001) 175–191.

[42] J. Szanyi, J.H. Kwak, D.H. Kim, S.D. Burton, C.H.F. Peden, J. Phys. Chem. B 109 (2005) 27–29.

[43] F. Prinetto, G. Ghiotti, I. Nova, L. Lietti, E. Tronconi, P. Forzatti, J. Phys. Chem. B 105 (2001) 12732–12745.

[44] B. Westerberg, E. Fridell, J. Mol. Catal. A: Chem. 165 (2001) 249–263.

[45] A. Lindholm, Kinetic Studies of NO_x Storage and Reduction Catalysts: Flow Reactor Experiments and Microkinetic Modeling, Department of Chemical and Biological Engineering, Chalmers University of Technology, Gothenburg, 2009.

[46] S. Kojima, N., Baba, S., Matsunaga, K., Senda, T. Itoh, SAE Technical Paper 2001-01-1297, 2001.

[47] J. Hepburn, E., Thanasiu, D., Dobson, W. Eatkins, SAE Technical Paper 962051, 1996.

[48] A. Casapu, J.D. Grunwaldt, M. Maciejewski, F. Krumeich, A. Baiker, M. Wittrock, S. Eckhoff, Appl. Catal. B–Environ. 78 (2008) 288–300.

[49] M. Piacentini, M. Maciejewski, A. Baiker, Appl. Catal. B–Environ. 66 (2006) 126–136.

[50] M. Piacentini, M. Maciejewski, A. Baiker, Appl. Catal. B–Environ. 72 (2007) 105–117.

[51] J.-S. Choi, W.P. Partridge, J.A. Pihl, M.-Y. Kim, P. Kočí, C.S. Daw, Catal. Today 184 (2012) 20–26.

[52] W.S. Epling, A. Yezerets, N.W. Currier, Catal. Lett. 110 (2006) 143–148.